*Journal of Global Positioning Systems (2012)*
*Vol.11, No.1 : 58-70*
*DOI: 10.5081/jgps.11.1.58*

Journal of Global Positioning Systems
2012
© CPGPS

# Detecting Severe Weather using GPS Tomography: An Australian Case Study

**Toby Manning[1], Kefei Zhang[1], Witold Rohm[1,2], Suelynn Choy[1], Fabian Hurter[3]**
[1] *Satellite Positioning for Atmosphere, Climate and Environment (SPACE) Research Centre, RMIT University, VIC, AUSTRALIA*
[2] *Institute of Geodesy and Geoinformatics, WUELS, Wroclaw, POLAND*
[3] *Geodesy and Geodynamics Laboratory, Institute of Geodesy and Photogrammetry, ETH Zurich, SWITZERLAND*

**Abstract**

The dynamics of water vapour (WV) has a strong influence on the formation and lifecycle of severe mesoscale convective storm systems due to the large energy transfers in the hydrological processes. Contrary to its importance WV remains poorly understood and inadequately measured both spatially and temporally, especially in the southern hemisphere where meteorological data are sparse. GPS meteorology is currently one of the most important atmospheric remote sensing instruments for meteorology and climatology due to its high spatial and temporal resolutions. Kalman filtering based GPS tomography is a promising method of reconstructing dynamically changing four dimensional (4D) wet refractivity fields. This method takes advantage of the high density and homogeneity of ground-based GPS Continuously Operating Reference Station (CORS) networks. Ground-based GPS tomography has the potential to utilize the dense ground-based infrastructure in Australia providing wet refractivity field solutions at a high spatial and temporal resolution to improve early detection and prediction of severe weather. This research presents a case study based on the analysis of an extreme convective super cell storm in the Victorian region during March 2010 using GPS tomography and the most advanced state-wide CORS network – GPSnet in Australia. Integrated Precipitable Water Vapour (PWV) estimates derived for the MOBS GPS CORS station confirmed high time resolution as well as sensitivity to incoming severe weather. A wet refractivity index adopted for GPS tomographic wet refractivity profiles shows an excessive increase as a response to supercell thunderstorm formation. Finally a 2D cross section mapping over the lifecycle of this severe weather event concludes a correlation between the highly dynamic spatial and temporal changes of wet refractivity modelled using 4D GPS tomography with precipitation intensities measured using weather radars.

**Keywords:** GPS; tomography; meteorology; severe weather; WV; wet refractivity

## 1. Introduction

Predicting the development and lifecycle of severe weather events such as thunderstorms is a highly complex process which at present has not been fully developed. The process is dependent on accurate measurements of water vapour (WV) distribution in time and space. The amount of water vapour contained in the troposphere also has significant implications for determining the strength and severity of a severe weather event (Choy, 2011). Contrary to this, WV remains poorly resolved especially in the southern hemisphere due to the lack of ground meteorological stations and low number of radiosonde launching sites.

In recent years GPS has been extensively used as a robust tool for measuring the integrated amount of WV in the atmosphere with high accuracy and under all weather conditions. It is currently regarded as one of the most important atmospheric remote sensing instruments for weather forecasting and climatology due to the rapidly increasing density of GPS CORS networks, the development of space-borne GPS technologies, and the continuous operability (Bevis et al., 1992; Ware et al., 1998; Tregoning et al., 1998; Gradinarsky, 2002; Le Marshall et al., 2010). The high spatial and temporal characteristics of GPS networks for meteorology complement the highly variable nature of severe weather and precipitation systems. The fundamentals of GPS tomography for reconstructing atmospheric wet refractivity fields has been demonstrated in multiple studies using Slant Wet Delays (SWD) as the input observables (Flores et al., 2000; Nilsson, 2005; Rohm, 2011, Van Baelen et al., 2011) and Double Differenced (DD) SWDs (Troller et al., 2006; Nicholson et al., 2005; Lutz, 2008; Perler et al., 2011).

Due to the sparse nature of ground-based atmospheric observation systems in the southern hemisphere the development of alternative methods for observing the spatial and temporal structure of the atmosphere is of high priority (Fu et al., 2009). Currently, the SPACE research centre and Australian Bureau of Meteorology's longstanding joint collaboration has provided the research platform for the implementation of space-borne GPS meteorological information into the current NWP model for Australia (Le Marshall et al., 2010). This study aims to incorporate ground-based GPS networks within Australia to investigate the signature of wet refractivity using GPS tomography during the influence of a severe weather event. A case study is presented which analyses the spatial and temporal dynamics of wet refractivity through a discretised model of atmosphere using tomography and the direct correlation with cumulative rainfall and the precipitation intensities of a convective super cell thunderstorm in Victoria during March 2010.

Detailed description of GPS signal refraction, GPS tomography principles and functional model of tomography is given in section 2. The fundamentals of severe mesoscale convective storm (MCS) systems and methods of using GPS to measure humidity sensitivity during these events including a new average wet refractivity index ($RI_{wet}$) is presented in section 3. A case study is presented with supporting results for a strong signature of WV distribution prior, during and after the severe weather event in section 4. This preliminary study is concluded in section 5, discussing implications of the results obtained, presenting recommendations and showing further steps in the GPS tomography research. The outlook of this research will look at developing a robust tomographic platform providing high spatial and temporal wet refractivity data in near real time, and assess the influence of additional observation systems including GPS radio occultation and radiosonde.

## 2. 4D Modelling of Wet Refractivity with GPS Tomography

GPS satellite signals are delayed and bent due to the variations in refractive index as they propagate through different layers of the atmosphere to a ground receiver. A linear combination of two frequencies can effectively eliminate the ionospheric component leaving the dry and wet effects of the troposphere represented as refractivity (Rueger, 2002).

$$N = N_{dry} + N_{wet} \quad (1a)$$

Where,

$$N_{dry} = 77.6890\frac{\mathrm{P_d}}{\mathrm{T}} \quad (1b)$$

$$N_{wet} = 71.295\frac{\mathrm{P_w}}{\mathrm{T}} + 375463\frac{\mathrm{P_w}}{\mathrm{T^2}} \quad (1c)$$

Where:

| | |
|---|---|
| $N$ | is the refractivity (ppm) |
| $\mathrm{P_d}$ | is the partial pressure of dry air (hPa) |
| T | is the atmospheric temperature (K) |
| $\mathrm{P_w}$ | is the partial WV pressure (hPa) |

The concept of GPS meteorology was first presented in Bevis et al. (1992) which proposed to utilise properties of the signal delays caused by the lower atmosphere and relate the magnitude of delays to the estimates of total zenith water vapour content or precipitable water vapour (PWV).

The GPS tomographic inversion process involves estimating the scalar field of wet refractivity values within a finite curvilinear grid from multiple integrated values passing through the media at different positions and orientations (Gradinarsky and Jarlemark, 2004). The key aspect in GPS tomography is a linear relation between path delays which are an integrated measure of signal delays, and, refractivity *N* within the finite voxel model, the same relation holds for dry and wet refractivity. The integration of refractivity *N* along the propagation path delay $\Delta^{SPD}$ between satellite x and receiver a can be expressed as (Troller et al., 2006):

$$\Delta^{PD}{}_{a}^{x} = 10^{-6}\int_{a}^{x} N \cdot ds = SHD + SWD \quad (2)$$

Where:

| | |
|---|---|
| $ds$ | is the line element along the ray path |
| $SWD$ | is the slant wet delay (m) |
| $SHD$ | is the slant hydrostatic delays |

Ray bending is neglected and a cut-off elevation angle of 5 degrees is used (Bender et al 2008).

The Bernese GPS processing software V5.0 (Dach et al., 2007) is used to attain the Zenith Total Delays (ZTD) and the DD phase residuals $\Delta\Phi_{a,b}^{x,y}$ using a shortest distance baseline strategy and a DD approach. A DD path delay observation can be reconstructed between 2 satellites (*x* and *y*) and 2 receivers (*a* and *b*) using the ZTDs from the receivers which are mapped to the corresponding elevations of the satellites using the Niell mapping function (Niell, 1996) $m(el_a^x)$ with the addition of DD residuals. In this study the wet refractivity is of interests, therefore the dry component is eliminated with high accuracy using additional ground meteorological observations at the GPS station using the dry Saastamoinen model (Saastamoinen, 1972). The final DD SWD equation (Troller et al., 2006) reads as follows:

$$\Delta^{2,SWD}{}_{a,b}^{x,y} = \overline{\Delta^{2,SWD}{}_{a,b}^{x,y}} + \Delta\Phi_{a,b}^{x,y} \quad (3)$$

Where,
$\overline{\Delta^{2,SWD}{}_{a,b}^{x,y}}$ is the isotropic double differences constructed using the isotropic wet slant path delays (Troller, 2006; Lutz, 2008 and Perler, 2011). This is expressed as:

$$\overline{\Delta^{2,SWD}{}_{a,b}^{x,y}} = \left(\overline{\Delta_b^{ZWD}} \cdot m(el_b^x) - \overline{\Delta_a^{ZWD}} \cdot m(el_a^x)\right) - \left(\overline{\Delta_b^{ZWD}} \cdot m\left(el_b^y\right) - \overline{\Delta_a^{ZWD}} \cdot m\left(el_a^y\right)\right). \quad (4)$$

DD SWDs are constructed and used as the input views through the finite voxel model by taking advantage of automatic elimination of the satellite and receiver clock biases (Ware et al., 1997; Troller et al., 2006; Lutz, 2008 and Perler et al., 2011).

For this study, 4D wet refractivity fields are processed using the Atmospheric Water Vapour Tomography Software 2 (AWATOS 2) which uses a Kalman filter for the forward processing, and *apriori* covariance and processing noises (Perler, 2011). Using a tri-linear parameterised field the algorithm of AWATOS 2 expresses the DD SWD observations as a weighted sum of the grid nodes (Perler et al., 2011).

$$\Delta^{SWD} = 10^{-6} \sum_i \int_{s_i}^{s_{i+1}} N_{wet,i} \Delta s_i \quad (5)$$

The tomography system of equation (5) is solved for wet refractivity using additional constraints in the form of pseudo observations. In the matrix form equation (5) with additional information as stated above, reads as follows (Lutz, 2008):

$$\begin{pmatrix} \Delta^{2,SWD}{}_{a,b}^{x,y} \\ ZWD_a \\ N_{apriori,i} \\ 0_i \end{pmatrix} = H \cdot \begin{pmatrix} N_{wet\ 1} \\ N_{wet\ 2} \\ N_{wet\ 3} \\ N_{wet\ 4} \\ N_{wet\ 5} \\ N_{wet\ 6} \\ \dots \end{pmatrix}. \quad (6)$$

Where:
$H$ is the design matrix.

A Kalman filter is used for this processing as it is highly advantageous for estimating the evolution of dynamically changing parameters. Previous studies have also incorporated a Kalman filtering technique to efficiently utilise the slant delay observations to obtain tomographic solutions (Flores, 2001; Gradinarsky and Jarlemark, 2004; Nilsson, 2005; Troller, 2006; Lutz, 2008 and Perler et al., 2011). The initialisation of the Kalman filter follows correlation parameters set in AWATOS 2 from Perler (2011) and an average wet refractivity profile from radiosonde profiles during the 7-day campaign.

## 3. Severe Mesoscale Convective Storm Systems and GPS Observations

Thunderstorms form in unstable atmospheric environments when warm, moist air rises due to instability of air masses. The warmer the parcel of air (less dense) the greater the acting upward-directed buoyant force and in turn the stronger the convection. The forcing mechanisms needed to start air moving upward may be: unequal heating at the surface; the effects of terrain, or the lifting of air along shallow boundaries of converging surface winds; diverging upper-level winds, coupled with converging surface winds and rising air; and, warm air rising along a frontal zone. Usually a combination of several mechanisms is needed together with vertical wind shear forces to generate severe thunderstorms (Ahrens, 2011). Supercell thunderstorms are uniquely characterised during the mature stage by the ratio of cold air downdraft being undercut by moist air updraft. This causes horizontal spin of a singular violent updraft which develops a supercell. These storms have the ability to suspend hailstones of considerable size, produce high speed winds and heavy precipitation, threatening safety, significant damage and flash flooding to communities. These mesoscale convective storm systems contain regions of both convective and stratiform precipitation. The convective region consists of intense, vertically extending cores, while the stratiform region hold a more stabilized lighter precipitation (Houze, 2004). See Fig. 1.

Preceding the heavy precipitation the storm becomes dominated by down draft. This process cuts off the inflow and updraft and the storm begins to dissipate (Ahrens and Samson, 2011). The fundamental elements of the storm structure require a much finer resolution where the mature cell and convective region can cover less than 30km. The stratiform on the other hand is much larger with a spatial coverage of 125km (Houze, 2004).

To identify the size, intensity and path of severe convective thunderstorms weather radar images are used. Radar signals are sent out as short pulses which may intercept elements such as precipitation and in turn scatter and reflect part of the energy back to the radar. From this returned information the radar is able to tell where the precipitation is occurring and how much precipitation exists. The intensity of precipitation is represented as a colour scale in a radar image and is based on the size, number and state of the particle (Masunaga, 2002).

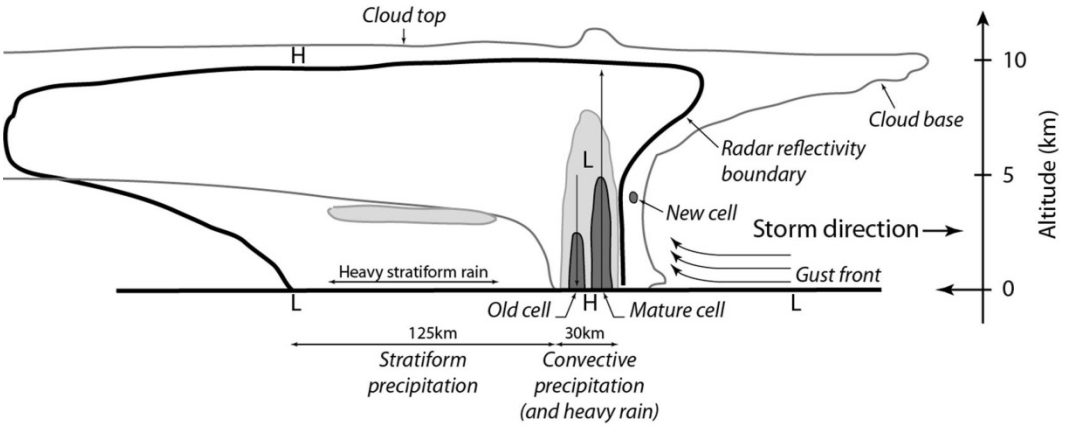


Figure 1: Profile view of a severe convective supercell thunderstorm. Radar reflectivity boundary identified and horizontal resolution of convective and stratiform precipitation regions (after Houze, 2004).

Radar images are able to detect the general domain of severe convective storm systems and depict the convective and stratiform precipitation regions. Figure 1 shows the extent of the storm that is able to be observed using radar imaging. The basic differences between radar images and tomography picture could be summarised as: 1) the wavelength of the signal, and 2) signal path. The radar pulse sent towards the MCS (5GHz frequency) is partially reflected by the rain drops, snow and ice crystals contained in all MCSs, whereas GNSS signals (1.5 GHz frequency) are refracted by the water vapour particles sustained in the air or moving upward, downward in air parcels and are afterwards recorded in GNSS receivers as phase delay. Therefore tomography images are available to picture both – increase of humidity before storm as well as decrease during the heavy rain.

The average refractivity index (RI), developed by Sharma (2009) is a measure of atmospheric instability using GPS RO derived refractivity measurements. The advantage of this index is the direct correlation with refractivity without retrieving temperature, pressure and water vapour measurements. The average value of refractivity (RI) is a mean of the values from height layers above the planetary boundary layer (PBL) (~2000m) to the tropopause. In this study we adopt RI and apply it to the wet refractivity profile computed using GPS tomography to produce a wet RI ($\mathrm{RI}_{wet}$) value. This optimizes the sensitivity to moisture content as it excludes the dominating dry component of refractivity (eq. 1a). The index is primarily used as an integral measure to identify early mechanisms of *lift* due to warm, moist air convection during the formation and lifecycle of severe weather through excessive and rapid increase and decrease of the index.

$$\mathrm{RI}_{wet} = \left(\sum_{l}^{k} N_{wet,l}\right) \Big/ n \qquad (7)$$

Where:
$l$ and $k$ represent the first and last $N_{wet}$ terms relating to the initial term above the PBL (~2000m) and the last term at the top of the tomographic model (15000m), respectively.

$n$ corresponds to the number of layer terms used. $n$ is set to 11 layer values as the voxel model discretization is fixed.

Furthermore, a 2D cross section is extracted from the tomographic solution along the path of the supercell storm analyzed for this case study. Gradient magnitudes denoting the dynamic wet refractivity field changes were calculated according to the equation:

$$\nabla 2\mathrm{D}N_{wet} = \left(\frac{\partial N_{wet}}{\partial x} i + \frac{\partial N_{wet}}{\partial h} k + \frac{\partial N_{wet}}{\partial t} p\right), \quad (8)$$

Where the first two elements denote the horizontal and vertical change in wet refractivity within one epoch, and last element denotes the time derivative of wet refractivity and only this element is being analyzed as a measure of troposphere activity parameter. These time evolving gradients are mapped against weather radar intensities to identify a trend of wet refractivity within the storm anomaly. A limitation in resolving the horizontal domains of a storm system is primarily due to the complexity of severe weather conditions and also the horizontal resolution that is constrained by the GPS network resolution. A much finer horizontal resolution would provide a much better data product for assisting in differentiation of storm regions, motion and intensity of supercell thunderstorms.

## 4. A Case Study: March 2010 Victorian Severe Weather Event

The focus of this case study is on the development and evolution of a series of supercell convective thunderstorms which passed through Victoria, Australia from 6 – 8 of March 2010 (Choy, 2011). This event brought heavy rainfall, lightning, flash flooding, strong winds and large hail stones. The storm was initiated by a large warm, humid air mass travelling from southern Queensland and developed in western Victoria due to a low pressure system. The unstable atmosphere developed into a severe supercell thunderstorm on the 6 March which travelled across the state from the northwest to the southeast. Warm, moist pre-frontal air was identified in the greater Melbourne region approximately 1 day prior to the event. At the storm's peak strength a 400km band of heavy rain and large hail extended across the state reaching Melbourne at approximately 14:40 AEDT (5:40 UTC). The synoptic weather station network revealed that the total rainfall for the day was the highest in historical record for March in Victoria. In Melbourne a total of 61 mm was measured for the 6 March, which is more than the monthly average of 50 mm. At approximately 14:40 (5:40 UTC) Melbourne experienced 19 mm in 18 minutes and 26 mm within 60 minutes. In addition, wind speeds in excess of 100 km/h and hail stones between 2 – 5cm were recorded throughout Melbourne (Choy, 2011). Figure 2 presents the radar reflectivity image from the Melbourne radar at 14:00, 14:48 and 15:24 AEDT (5:00, 5:48, and 6:24 UTC) on 6 March 2010 as the storm passed over central Melbourne. This event caused danger to civilians, flash flooding, immense commercial and residential damage, and vast traffic and transport delays. Further rain and flash flooding continued throughout the night and into 7 March.

It can be seen that the storm region of highest precipitation denoted by dark-red passes directly over central and greater Melbourne during this period.

### 4.1 Ground-based GPS meteorology

The Victorian GPS CORS network currently comprises approximately 105 dual-frequency geodetic grade GPS receivers in continuous operation from which 69 were available in March 2010 and used for this research. Mean inter-station distance is approximately ~70 km with a reasonably homogeneous distribution. The network is highly dense for Australian standards and has the potential to be a major resource for meteorological data especially in the absence of sufficient meteorological observation systems and increase the ability to resolve the spatial and temporal evolution of severe weather.

GPS PWV estimates are constructed using the zenith total delays (ZTD) calculated as part of the stochastic filtering during GPS data processing. Using the surface pressure measurements from synoptic weather stations and the associated geoid height (H) and geographic latitude (φ) of the GPS station (a) the hydrostatic or dry components of the delay at the zenith (zenith hydrostatic delay) can be computed and eliminated using the Saastamoinen hydrostatic equation (Saastamoinen, 1972). This leaves the ZWD ($\Delta_a^{ZWD}$) which can be converted into PWV using a mean temperature value in a conversion factor $\Pi$ (Bevis et al., 1992).

Figure 3 presents an analysis study of the evolution and comparison between GPS PWV and cumulative rainfall measurements 3 days prior to, during, and 3 days after this extreme thunderstorm. The data represents observations from the Melbourne observatory (MOBS) station.


Figure 2: Radar reflectivity image from the Melbourne radar (Laverton) at 14:00, 14:48 and 15:24 (AEDT) (5:00, 5:48, and 6:24 UTC) on 6 March 2010 (source BoM).

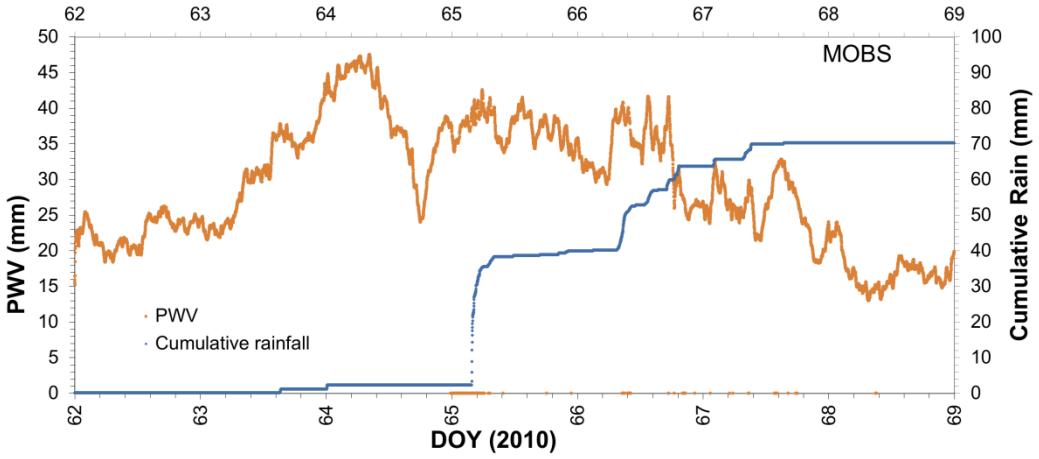


Figure 3: Time series comparing GPS PWV (mm) to the cumulative rainfall (mm) over the 7 day case study campaign (AEDT).

The large increase from 20 mm to 47 mm (PWV) from day-of-year (DOY) 63 to 64 corresponds to the steady increase in warm moist air attributed to a pre-frontal air mass. Pre-frontal warm air holds more WV than the cold post-frontal air (Choy, 2011). Thus, Figure 3 presents this clear signature of increasing PWV to 47 mm representing the warm pre-front air and the immediate atmospheric procession of a sharp drop back to approximately 23 mm characterising the arrival of cold, dry post-front air mass. Validation of the PWV estimates from GPS with radiosonde concluded an overall RMS error of 2-3 mm (PWV) for greater Melbourne (Choy, 2011). This initial result identifies the ability of GPS state-wide networks to map the passage of integrated water vapour in the pre- and post-frontal air mass with a high spatial and temporal resolution continuously in the outlook for severe weather.

The GPS PWV is an integral estimation of the total WV content in a column above MOBS GPS station. To reconstruct a vertically resolved WV field GPS tomography is proposed. By applying a tomographic inversion method (eq. 6) to GPS slant wet delays (eq. 2) it is possible to reconstruct vertically resolved wet refractivity of a finite grid model. The solution provides vertically resolved profiles at every base grid point, with a horizontal resolution of 0.5° GPS observation temporal resolution of 30 seconds and an update step size of 5 minutes.

### 4.2 Tomography analysis

This analysis presents a new platform in Australia and initially Victoria for the improvement of forecasts of precipitation and severe weather using GPS tomography. The spatial and temporal resolutions are imperative parameters for optimising the depiction of hydrological hazards using highly dynamic WV modeling (Lutz, 2008). The resolution of the discretised 3D field, the Kalman filter parameters and update resolution for AWATOS 2 processing are set for this research based on simulation studies in Victoria (Manning et al., 2012) and results from real data processing by Perler (2011).

The discretisation of the lower atmosphere is defined with a finite curvilinear voxel grid using latitude and longitude boundaries referenced to the WGS84 ellipsoid. The area under investigation ranges from $141^0$ - $148^0$ E longitude and $-35.8^0$ to $-38.6^0$ S latitude with a height domain from 0 – 15000 m (Fig. 4b). Furthermore, a buffer of $10^0$ borders the outside of this model domain to ensure that all rays are within the model and pass through the top boundary. The horizontal resolution at the surface is set to $0.5^0$ (Fig. 4a) which is approximately the overall diameter size of the super cell thunderstorm and is slightly denser than the inter station GPSnet distance of 70 km which is the suggested voxel adoption following the preconditions of GPS tomography from Bender (2007). To provide an optimal tomographic output to assist in the depiction of the segmented dynamics of the individual convection and stratiform domains of a severe supercell storm using NWP a much finer horizontal resolution would be needed. However, this discretisation is limited by the resolution of the GPS CORS network where an increase in the number of unknowns in equation 6 does not add additional observations and ultimately, in the presence of horizontal constraints a smoothing effect is generated. Approximately 50% of water vapour is located in the PBL making it imperative to model the dynamic and vertical structure of WV below ~2000 m with a high resolution. Therefore, the vertical resolution is set to 15 layers with exponential layer spacing as presented in Figure 4b. This produces a high resolution in the lower troposphere and a low resolution in the upper troposphere (Lutz, 2008 and Perler, 2011).

GPS data from the Victorian GPS CORS network (see Fig. 4a) was processed using the Bernese GPS processing software V5.0 (Dach et al., 2007) using a shortest distance baseline strategy and a DD approach. The estimated hourly Zenith Path Delay (ZPD), the DD residuals, interpolated meteorological data from Numerical Weather Prediction model ACCESS-R (Le Marshall et al., 2010) and satellite and receiver coordinates are used to reconstruct the DD SWD (eq. 3) observations which are the primary input for the tomography inversion during each update step of the Kalman filter. The initialization of the Kalman filter uses correlation parameters set in AWATOS 2 from Perler (2011) along with an initial exponential vector state modelled on average wet refractivity profiles from radiosondes during the 7 day campaign and variance estimates. The data sampling size is set to 30 seconds and the update step size set to 5 minutes. Vertical constraints and boundary layer conditions are supplied to the observation matrix (eq. 6) as pseudo-observations.

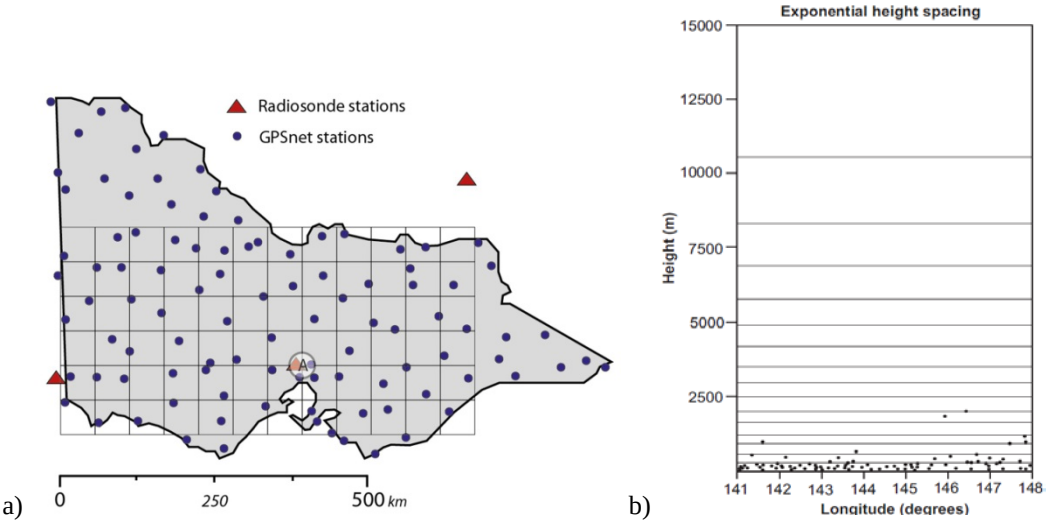


Figure 4: The Victorian GPSnet CORS network, radiosonde sites, horizontal discretization of the grid model and grid corner A selected for analysis (a), and, vertical layer structure defined with an exponential spacing technique (b).

### 4.3 Results and discussion

The formation of a convective storm system must involve three conditions. The first is *moisture* in the lower to mid troposphere. The second is atmospheric *instability* which can be a good indicator for storm intensity. The last condition is a collaboration of *lift* mechanisms. This preliminary analysis identifies the signature of wet refractivity during the early formation of the convective storm using 4D GPS tomography. Wet refractivity is a function of partial WV pressure and temperature (eq. 1c).

Figure 5 presents the evolution of the tomographic wet refractivity profile solution at grid profile point (A) (see Fig. 4a) over the 7 day campaign. The cumulative rainfall is scaled to the right y-axis with the supercell storm period identified. The evolution of $RI_{wet}$ index is presented below along the same time series. An $RI_{wet}$ index of 12.73 ppm is adopted as a standard value for a stable atmosphere, derived using radiosonde profiles from the Melbourne Airport station for the month of March 2010 excluding the 7 day storm period.

The $RI_{wet}$ index presents an approximately linear rise from day of year (DOY) 63 to 64.3 coinciding with the large amounts of warm, moist air and the process of strong *lift* or convection in the pre-frontal, unstable atmosphere. This process is consistent with the large warm, humid air mass detected moving down from southern Queensland which triggered the atmospheric instability. The index reaches 28 ppm approximately 2.3 times greater than the standard atmospheric index. This is preceded by a dry, cold post frontal air triggering a sharp drop in the index and then a sharp rise until the heavy rainfall, hail and flash flooding reaches Melbourne. The tomographic profile evolution presents a similar signature to the $RI_{wet}$ index. However, the highly dynamic distribution of wet refractivity in the vertical direction is detected with periods revealing distinct patterns of convective updraft due to warm moist air and instability. Also periods of cool, dry air are detected – represented by sharp drops down the vertical layers due to cold air mass advection, and, during the mature and dissipating storm lifecycle phase due to heavy precipitation.

The tomographic analysis was validated with radiosonde profiles from the Melbourne International Airport coinciding with profile point (A) in Figure 4. The radiosonde station provides 2 profiles per day with14 in total for comparison. A tomographic solution every 12 hours was selected and presented in Figure 6a to coincide with the temporal resolution of the radiosonde. Figure 6b presents the vertical colour map for the time evolving radiosonde profiles against the cumulative rainfall data. Due to the low temporal resolution the signature and distribution of wet refractivity remains poorly resolved. The $RI_{wet}$ index is interpolated and computed for the same height layers as the tomographic solution and presented below. The colour map in Figure 7 presents the difference between radiosonde and tomography profiles at the collocated Melbourne International Airport site. The RMS error for each profile comparison is acceptable and consistent considering the highly unstable nature of WV within the model field during the severe weather event. An overall RMS error of 7.8 ppm was achieved with the highest being 11.1 ppm.

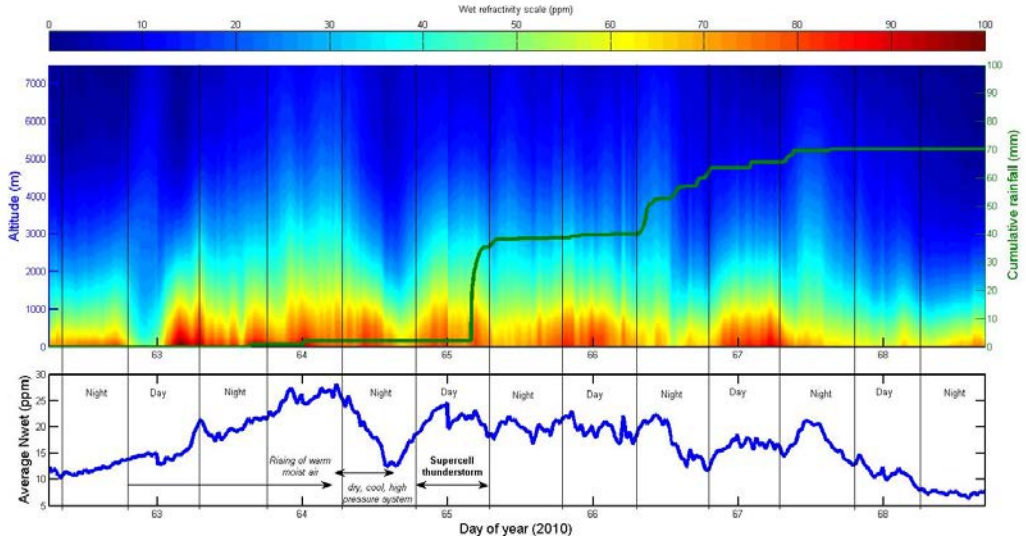


Figure 5: Evolution of tomographic profile solutions of wet refractivity every 10 minutes 3-8 March 2010 (UTC). Green line presents cumulative rainfall (mm) from MOBS synoptic station during this period. Below is the evolution of the $RI_{wet}$ index.

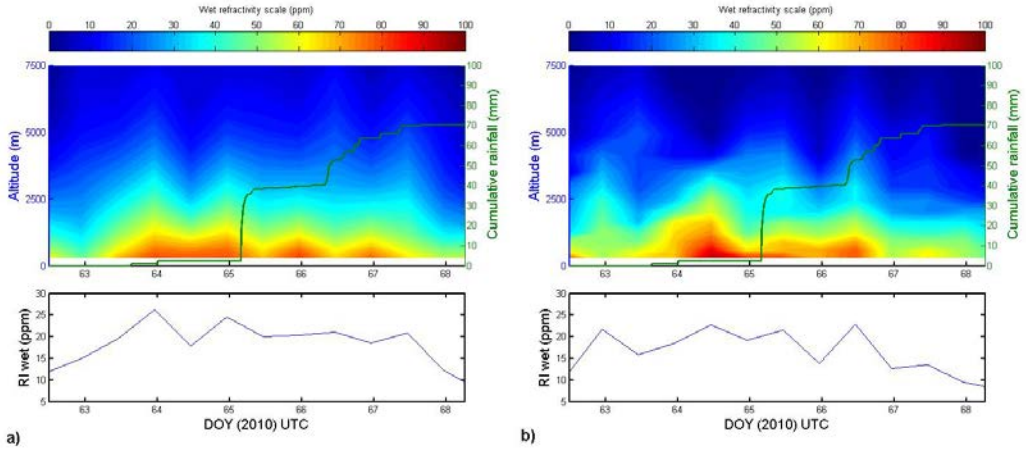


Figure 6: Evolution of tomographic profile solutions of wet refractivity every 12 hours with $RI_{wet}$ index profile (a), and, evolution of radiosonde profiles with 12 hour resolution from the Melbourne Airport station including $RI_{wet}$ index profile (b). Green line represents cumulative rainfall (mm) from the 3-8 March 2010 (UTC).

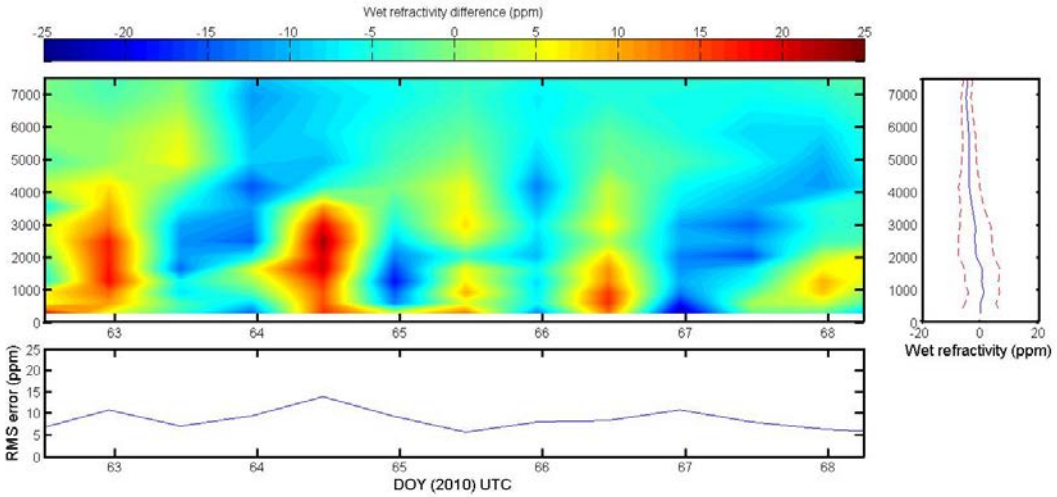


Figure 7: Wet refractivity of radiosonde minus tomography profile at the Melbourne International Airport every 12 hours. RMS error of each profile solution (below) and the bias and Standard deviation at each height layer (right).

Only 3 radiosonde stations operate within greater Victoria and each function on a 12 hour temporal resolution. Figure 8 presents the comparison between the radiosonde and tomographic $RI_{wet}$ index. The major difference between the two data sets is the much higher temporal resolution of tomography which provides a solution every 5 minutes. Comparing the radiosonde and tomography $RI_{wet}$ index values concluded an accuracy of 3.8ppm (RMS).

The bias and standard deviation at each height layer is displayed in the profile on the right (see Fig. 7) with overall values of 1 ppm and 6.2 ppm, respectively. The majority of variability is present below ~4000 m which would be expected especially during severe weather due to the highly variant nature of water vapour in an unstable atmosphere.

Due to the sparse spatial and temporal nature of the radiosonde network can be concluded that this data product alone is insufficient for comprehensive resolvability of the physical dynamics of water vapour during severe weather which limits the ability for early detection and prediction. The $RI_{wet}$ index comparison (see Fig. 8) illustrates the limitations of radiosonde profiles revealing the inability to depict sharp temporal changes associated with convection and mechanisms of *lift* for wet refractivity in an unstable atmosphere. An example of this is the pre- and post- frontal air anomaly during DOY 64 where the tomography solution provides a highly variant time series, whereas the dynamic changes of the atmospheric anomaly remain totally unresolved using radiosonde profiles.

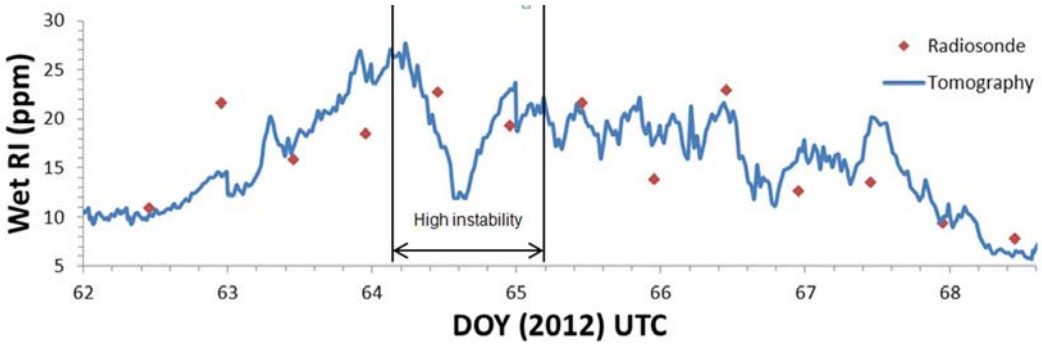


Figure 8: Average wet refractivity index (RI) for radiosonde and tomography profiles at respective temporal resolutions of 720 and 10 minutes, respectively. High instability domain indicated.

A 2D cross section is extracted from the tomographic solution to spatially and temporally depict the generalised pattern of wet refractivity dynamics during a MCS system. The path and precipitation intensity of the March 2010 supercell storm is presented using a colour scale of the weather radar intensity at hourly intervals

(see Fig. 9). Figure 9 presents the lifecycle and direction of this supercell convective storm from formation to dissipation. The grid points depict the tomographic resolution used to discretise the atmosphere and the red circles present the area of interpolation for the radar image intensity. The diagonal tomographic grid profiles are select to reconstruct a 2D profile for comparison with the radar intensity. The theoretical size and dynamics of MCSs suggests that a much finer horizontal resolution than used for this tomography is needed to conclusively depict the small scale convective dynamics and mature cell of the storm (see Fig. 1). This limitation is constrained by the resolution of the GPSnet CORS network.

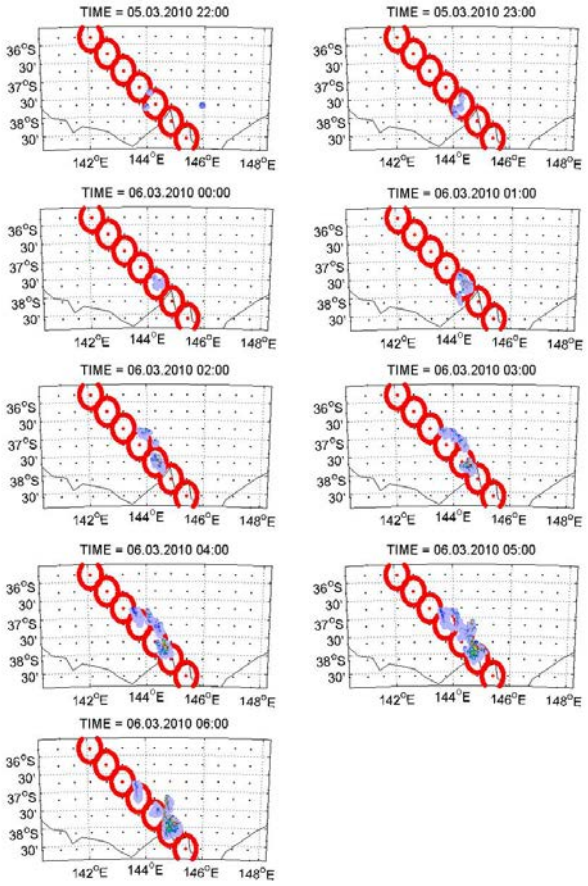


Figure 9: Tomographic domain presented with black dots corresponding to grid corners, red dots presenting profile grid points used to construct the tomographic 2D cross section, weather radar image intensity, and, red circles representing the interpolation domain for the weather radar image. The time series from 5 Mar 2010 22:00 to 6 Mar 2010 06:00 (UTC) presents the lifecycle of the extreme supercell thunderstorm passing over greater Melbourne.

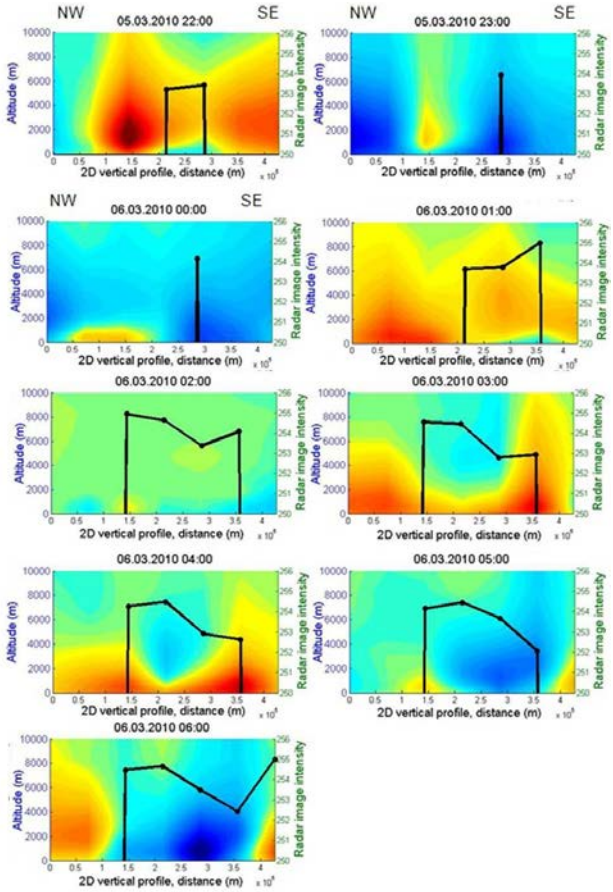


Figure 10: The time series from 5 Mar 2010 22:00 to 6 Mar 2010 06:00 (UTC) presenting 2D tomographic cross section against the weather radar image intensity.

Figure 10 presents the time evolving tomographic solution gradients along the cross section profile with the interpolated radar image intensity mapped to the y-axis (right). A 9 hour section of processing is presented from 22:00 on 5 Mar 2010 UTC (7:00 on 6 Mar 2010 AEDT) to 06:00 on 6 March 2010 UTC (15:00 on 6 Mar 2010 AEDT) at hourly intervals. The storm motion is from the NW to SE. As the convective system matures the precipitation domain increases in size and intensity. The major trends evident in the time series are the areas of intense precipitation that show a distinct drop in wet refractivity over all layers and especially in the mid troposphere. Furthermore, regions in front of the storm path present a large increase in wet refractivity gradients up through each layer. This dynamic trend at the front of the storm depicts the convection process of warm, moist air in the violent updraft of the gust front and formation of the mature cell (see Fig. 1). This is particularly evident from 03:00 to 05:00 (UTC) on 6 Mar 2010 as the supercell storm reaches greater Melbourne with 26mm of rain falling within 60 minutes and record precipitation totals recorded for this day. The cross sections from 03:00 to 04:00 UTC at the front of the radar intensity

show very strong gradient increases through all layers up to 10,000m altitude and especially in the mid to low troposphere. Gradient increases in wet refractivity from tomography are also evident behind the storm precipitation system and stratiform region depicted using the radar intensities. This coincides with dissipation of the storm beyond the stratiform precipitation in a stabilizing atmosphere and the melting and evaporation of precipitation parcels in the stratiform clouds (Houze, 2004).

These findings demonstrate that GPS meteorology and more recently GPS tomography have the capability to provide state wide and potentially national continuous observations to contribute to early detection and prediction of severe weather.

## 5. Conclusion and outlook

This research presents a new observational platform in Australia using GPS tomography for the improvement of early detection and prediction of severe weather. The results from this case study indicate a strong correlation between the evolutions of wet refractivity fields derived using 4D GPS tomographic solutions and the lifecycle of a severe convective thunderstorms depicted using weather radar intensities. The Kalman filter based tomography package AWATOS 2 (Perler, 2011) was used to reconstruct the dynamics of wet refractivity with update solutions every 5 minutes. The advantage of using the GPS CORS networks for meteorology is the high spatial and temporal resolution compared with other ground-based atmospheric sounding instruments.

The tomography solution was validated against radiosonde profiles collocated at the Melbourne International Airport. The RMS error is consistent throughout the 7 day campaign considering the highly unstable nature of WV within the model field during the severe weather event. An overall RMS error of 7.8 ppm was achieved. An average wet refractivity index ($RI_{wet}$) was computed from the tomography solution which provides a WV and temperature sensitive index for identifying excessive increases during mechanisms of convection and lift during the early formation of severe convective storms. The index was also applied to collocated height layers of the radiosonde profiles and compared with tomographic $RI_{wet}$ index to conclude an accuracy of 3.8 ppm (RMS). The advantage of this index is the high sensitivity of GPS signal propagation to increased fluctuations of WV which translates into the tomographic solution and in turn signifies large fluctuations of the $RI_{wet}$ index. This is especially evident during the pre- and post- frontal air mass prior to the severe supercell thunderstorm.
A 2D cross section analysis revealed a high correlation between the tomographic solution and precipitation intensities measured using weather radars. High positive wet refractivity time gradients were evident in front of the storm suggesting high levels of humid convection and immediate reduction in gradients in regions of significant precipitation intensities due to heavy rain.
These findings are very positive as GPS tomography solutions can be used as an additional meteorological observation source with relatively high spatial and temporal resolution for early detection and prediction of severe weather events.

**Acknowledgements**

This project is supported by the Australian Space Research Project (ASRP) and by the Australian Research Council (ARC) Linkage (LP0883288) project both funded by the Australian Federal Government. We also thank the Geodesy and Geodynamics Lab, ETH Zurich, Switzerland for providing the AWATOS 2 software package, the Australian Bureau of Meteorology for providing the synoptic weather station and radiosonde data, and, the Department of Sustainability and Environment for providing the GPSnet data.

## References

Bai Z. (2005), ***Near-Real-Time GPS Sensing of Atmospheric Water Vapour***, PhD thesis, Queensland University of Technology.

Bender M. and A. Raabe (2007), ***Preconditions to ground-based GPS water vapour tomography***, Ann. Geophys., Vol. 25 No.8, pp. 1727–1734.

Bender M., G. Dick, J. Wickert, T. Schmidt, S. Song, G. Gendt, M. Ge, and M. Rothacher (2008), ***Validation of GPS slant delays using water vapour radiometers and weather models,*** Meteorologishe Zeitschrift Vol. 17, No. 6 pp.807–812.

Bevis M., S. Businger, T. Herring, C. Rocken, R. Anthes, and R. Ware (1992), ***GPS Meteorology: Remote Sensing of Atmospheric Water Vapor Using the Global Positioning System***, J. Geophys. Res., Vol. 97, No. 15, pp. 787-801.

Champollion C., F. Mason, M. Bouin, A. Walpersdorf, E. Doerflinger, O. Bock, and J. van Baelen (2005), ***GPS water vapour tomography: preliminary results from the ESCOMPTE field experiment***, Atmospheric Research, Vol. 74, pp. 253-274.

Choy S., K. Zhang, C. Wang, Y. Li, and Y. Kuleshov (2011), ***Remote Sensing of the Earth's Lower Atmosphere during Severe Weather Events using GPS Technology: a Study in Victoria, Australia***,

ION GNSS 2011, Portland, Oregon, USA, 20-23 September.

Dach R., U. Hugentobler, and P. Fridez (2007), ***Bernese GPS Software Version 5.0***, Astronomical Institute, University of Bern, Bern.

Flores A., G. Ruffini, and G. Rius (2000), ***4-D tropospheric tomography using GPS slant wet delays***, Annales Geophysicae, Vol. 18, pp. 223-234.

Fu E., K. Zhang, K Marion, X. Xu, J. Marshall, A. Rea, G. Weymouth, and Y. Kuleshov (2009) ***Assessing COSMIC GPS radio occultation derived atmospheric parameters using Australian radiosonde network data***, The 6th International Conference on Mining Science & Technology, Procedia Earth and Planetary Science 1.

Gradinarsky L. (2002), ***Sensing atmospheric water vapor using radio waves***, Ph.D. dissertation, Chalmers University of Technology, Technical report No 436.

Gradinarsky L., and Jarlemark P. (2004) ***Ground-based GPS tomography of water vapour: Analysis of simulated and real data***, J. Meteorol. Soc. Japan Vol. 82 pp. 551–560.

Grewal M., and L. Weill (2002), ***Frontmatter and Index. Global Positioning Systems, Inertial Navigation, and Integration***, John Wiley & Sons, Inc.: i-xxi., pp. 1054–1059.

Houze (Jr) R. (2004) ***Mesoscale convective systems***. Reviews of Geophysics, Vol. 42, RG4003.

Le Marshall J., Y Xiao, R. Norman, K. Zhang, A. Rea, L. Cucurull, R. Seecamp, P. Steinle, K. Puri, and T. Le (2010), ***The beneficial impact of radio occultation observations on Australian region forecasts***, The Australian Meteorological and Oceanographic Journal (AMOJ), Vol. 60, pp 121-125.

Hajj G., E. Kursinski, L. Romans, W. Bertiger, and S. Leroy (2002), ***A technical description of atmospheric sounding by GPS occultation***, Journal of Atmospheric and Solar-Terrestrial Physics, Vol. 64, No. 4, pp. 451-469.

Lutz S. (2008), ***High-resolution GPS tomography in view of hydrological hazard assessment***, PhD thesis No. 17675, ETH Zurich, Switzerland.

Manning T., W. Rohm, K. Zhang, F. Hurter, and C. Wang (2013), ***Determining the 4D dynamics of wet refractivity using GPS tomography in the Australian region***, IAG Symp. 139 (accepted Dec. 2012).

Masunaga H., T. Iguchi, R. Oki, and M. Kachi (2002), ***Comparison of Rainfall Products Derived from TRMM Microwave Imager and Precipitation Radar***. J. Appl. Meteor, Vol. 41, pp. 849–862.

Niell A. (1996), ***Global mapping functions for the atmospheric delay at radio wavelengths***, J. Geophys. Res., Vol. 101, pp. 3227- 3246.

Nilsson T. (2005), ***Assessment of tomographic methods for estimation of atmospheric water vapor using ground-based GPS***, PhD thesis, Chalmers University of Technology, Göteborg, Sweden.

Nicholson N., S. Skone, M. Cannon, G. Lachapelle, and N. Luo (2005), ***Regional tropospheric tomography based on real-time double difference observables***, Proceedings of ION GNSS 2005, Long Beach, California, U.S.A, pp 269-280.

Perler D., A. Geiger, and F. Hurter (2011), ***4D GPS water vapor tomography: New parameterized approaches***. Journal of Geodesy, 10.1007/s00190-011-0454-2.

Perler D. (2011), ***Water vapour tomography using global navigation satellite systems***, PhD thesis No. 20012, ETH Zurich, Switzerland.

Rohm W, and J. Bosy (2011), ***The verification of GNSS tropospheric tomography model in a mountainous area***, Advances in Space Research. Vol. 47, pp. 1721-1730.

Rueger J. (2002), ***Refractive index formulae for electronic distance measurement with radio and millimetre waves,*** School of Surveying and Spatial Information Systems, University of New South Wales, Unisurv Rep. S-68, pp 13.

Saastamoinen J. (1972), ***Atmospheric correction for troposphere and stratosphere in radio ranging of satellites***. In: Henriksen SW, Macini A, Chovitz BH (eds) The use of artificial satellites for geodesy. Geophysics monograph, vol 15. American Geophysical Union, Washington D.C. pp 247–251.

Sharma N., D. Jagadheesha, P. Joshi, and P. Pal (2009), ***Atmospheric stability estimation using radio occultation data over India and surrounding region***, Indian Journal of Radio and Space physics. Vol. 38, pp. 317-325.

Tregoning P., R. Boers, and D. O'Brien (1998), ***Accuracy of absolute precipitable water vapor estimates from GPS observations***, Journal of Geophysics. Res. Vol. 103 (28), pp. 701-719.

Troller M., A. Geiger, E. Brockmann, and H. Kahle (2006), ***Determination of the spatial and temporal variation of tropospheric water vapour using CGPS networks***, Geophys J Int Vol. 167(2), pp. 509–520.

Van Baelen J., M. Reverdy, F. Tridon, L. Labbouz, G. Dick, M. Bender, and M. Hagen (2011), ***On the relationship between water vapour field evolution and the life cycle of precipitation systems***, Quarterly Journal of the Royal Meteorological Society, Vol. 137, pp. 204–223

Ware R., C. Alber, C. Rocken, and F. Solheim (1997), ***Sensing integrated water vapor along GPS ray paths***, Geophys. Res. Lett., Vol. 24, pp. 417– 420.

**Biography**

Toby Manning is a PhD candidate with the SPACE research centre, RMIT University, Melbourne, VIC, Australia. His main area of research is the study of GPS tomography in the Australian region with particular interest in analysis during severe weather. his email is toby.manning@gmail.com.